Conformal Integration of an Inkjet-Printed PbS QDs-Graphene IR Photodetector on a Polymer Optical Fiber

Gökhan Kara, Sami Bolat, Khushdeep Sharma, Matthias J. Grotevent, Dmitry N. Dirin, Dominik Bachmann, Roman Furrer, Luciano F. Boesel, Yaroslav E. Romanyuk, René M. Rossi, Maksym V. Kovalenko, Michel Calame, and Ivan Shorubalko*

Hybrid graphene-colloidal PbS quantum dots (QDs) phototransistors are promising to overcome the geometrical restrictions of photodetectors to flat substrates. While compatible with conformal manufacturing, the experimental demonstration of their application to curved surfaces remains elusive. This work demonstrates the seamless integration of an infrared (IR) photodetector to a polymer optical fiber (POF) by wrapping graphene around the POF of 1 mm in diameter and, subsequently, inkjet printing of PbS QDs onto the curved surface. The device acts as a functional coating and detects infrared light propagating through the POF without interrupting the waveguide. The formulated α-terpineol and hexane co-solvent ink supports drop-on-demand placement with a resolution of 50 μm and is colloidally stable over 7 months. A responsivity map over gate voltage and temperature (300 to 80 K) of a device, fabricated on a common flat substrate, reveals a responsivity of $R \approx 1 \times 10^3 AW^{-1}$ (irradiance ≈ 1 μW cm^{-2}) and a detectivity of $D^* \approx 1 \times 10^{10}$ Jones at 1.6 μm wavelength. This work brings the integration of this cost-effective and adaptable hybrid detector approach closer to multifunctional e-textiles and will, notably, help to improve the interfacing of the skin as desired for wearable and non-invasive healthcare applications.

1. Introduction

Wearable electronics is drawing considerable attention to healthcare applications for monitoring vital signs and beyond.[1–3]

Near (NIR) to shortwave (SWIR) infrared optical imaging, in particular, is used to assess the oxygen arterial saturation by quantifying the ratio of oxyhemoglobin to deoxyhemoglobin. The benefit of reduced tissue absorption in this spectral range (biological window: 700–1400 nm)[4] enables non-invasive direct probing.[1,5] First, flexible but flat detector concepts reveal the potential of an improved adaption to the skin and are based on organic[6] or hybrid graphene-colloidal PbS quantum dots (QDs)[7] materials. E-textiles based on smart fibers further improve interfacing the skin by reducing the structure dimension (from 2D flat substrate to 1D fibers)[8] and demonstrate their potential for energy harvesting and storage, light emission, as well as sensing applications.[9–14]

Optimally, an e-textile allows for the integration of a diverse set of functionalities to, for instance, assess different vital signs as predictors of the overall health status of an individual. This requires the integration of multiple functions to a single fiber and poses a distinct need for new technological approaches. Methods to integrate IR detectors locally and on curved surfaces are, thus, highly desired. The combination of low-dimensional nanomaterials, such as

---

G. Kara, M. J. Grotevent,[+] D. Bachmann, R. Furrer, M. Calame,
I. Shorubalko
Laboratory for Transport at Nanoscale Interfaces
Empa – Swiss Federal Laboratories for Materials Science and Technology
Dübendorf CH-8600, Switzerland
E-mail: ivan.shorubalko@empa.ch

The ORCID identification number(s) for the author(s) of this article can be found under https://doi.org/10.1002/admt.202201922.

[+]Present address: Department of Chemistry, Massachusetts Institute of Technology, Cambridge, MA 02139, USA

S. Bolat, Y. E. Romanyuk, M. V. Kovalenko
Laboratory for Thin Films and Photovoltaics
Empa – Swiss Federal Laboratories for Materials Science and Technology
Dübendorf CH-8600, Switzerland

K. Sharma, L. F. Boesel, R. M. Rossi
Laboratory for Biomimetic Membranes and Textiles
Empa – Swiss Federal Laboratories for Materials Science and Technology
St. Gallen CH-9014, Switzerland

M. J. Grotevent, D. N. Dirin, M. V. Kovalenko
Department of Chemistry and Applied Biosciences
ETH – Swiss Federal Institute of Technology Zurich
Zurich CH-8093, Switzerland

M. Calame
Department of Physics and Swiss Nanoscience Institute
University of Basel
Basel CH-4056, Switzerland

graphene and colloidal QDs, with inkjet printing is recognized as a promising route for conformal manufacturing.[15–18] Solution processable colloidal QDs are, however, commonly deposited by spin coating, dip coating, or drop-casting. These methods are not suited for spatially well-defined sensitization or deposition on 3D-curved objects. Inkjet printing, as an alternative, benefits from drop-on-demand placement. The ink formulation is challenging and goes well beyond tuning rheological properties for stable droplet formation. To promote this technology to practical applications, long-term colloidal stability of the QDs, as well as tackling ink substrate interactions is essential. Interesting demonstrators of printed infrared photodetectors based on HgTe and PbS QDs have been shown in the literature by inkjet printing[19–22] or electrohydrodynamic nanoprinting (EHD),[23–25] but are generally restricted to flat substrates. With EHD printing, small feature sizes of ≈ 1 μm can be achieved at the cost of printing speed (≈μm s⁻¹).[23] Thus, conventional inkjet printing is preferred in this case despite the lower resolution. Although there are first curved photovoltaic detectors based HgTe QDs reported in the literature,[26] they are fabricated on flat substrates initially, and the precise placement of QDs films remains still open. One challenge to realize printing on curved objects lies in adequate droplet pinning and depends on droplet-substrate interaction. It is determined by surface tension and, in addition, the shape and motion evolution of the drops along the incline.[27,28] The interplay governs the wetting and dewetting of the surface and is responsible for the deposition of active material on the curved surface. Furthermore, graphene, which is known as one of the most flexible materials, can be integrated on curved surfaces for transparent conductive layers, for example, in lenses.[29,30] This often requires an elaborate processing scheme and specific supporting structures limiting the substrate choice.

Here, we demonstrate technology for the fabrication of hybrid graphene-PbS QDs IR phototransistors on a curved surface by inkjet printing. First, we examined the printing of PbS QDs with neat hexane versus a formulated co-solvent ink composed of an α-terpineol and hexane mixture. The latter combination allows stable drop-on-demand pattern printing with well-resolved features of 50 μm. Moreover, the ink retained colloidal integrity for at least 7 months. The photoresponse in hybrid graphene-PbS QDs detectors was first tested on devices fabricated on common flat substrates (p-Si/oxide). The responsivity maps over gate voltage and temperature (300–80 K) confirmed a photosignal sign change, previously reported for this device architecture.[24] Then, the hybrid photodetector was seamlessly integrated to a polymer optical fiber (POF) as a first step toward smart textiles. Graphene was wrapped around a POF of 1 mm in diameter, followed by inkjet printing of PbS QDs on the curved surface. This functional coating detects coupled light into the POF without interrupting the light path. Integrating such smart fibers into e-textiles can potentially improve non-invasive IR probing for healthcare applications tremendously.
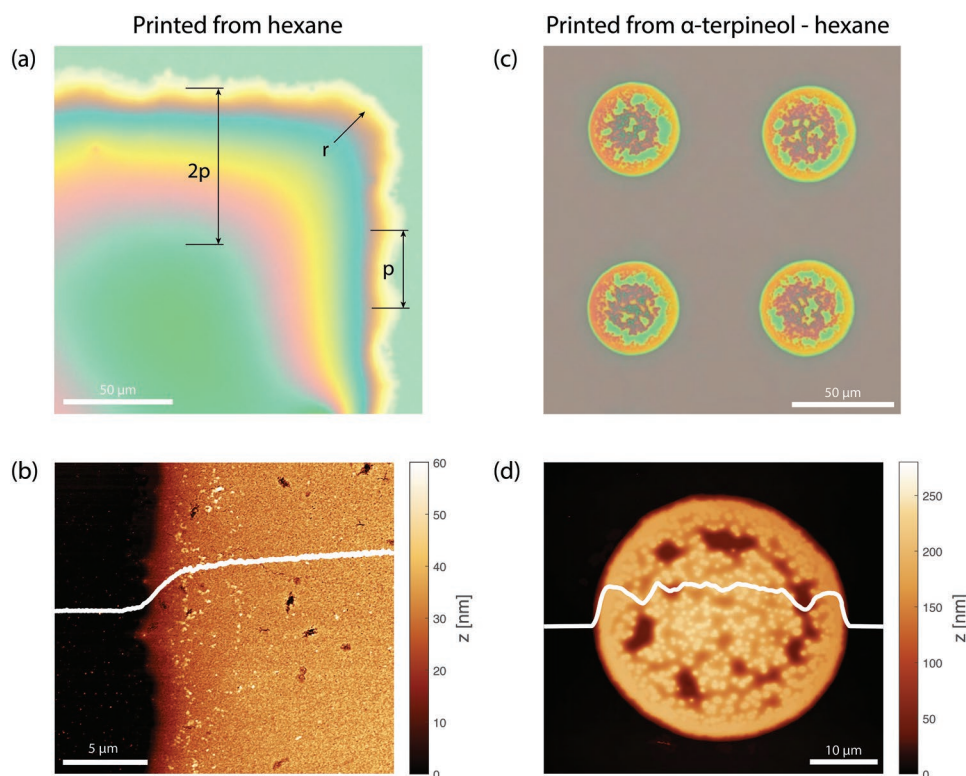
2. Results and Discussion

2.1. Colloidal PbS QDs Ink Formulation

Drop-on-demand inkjet printing requires the ejection of a single drop after each applied piezoelectric pulse. The formation of satellites (tiny droplets following the main drop) should be suppressed to achieve well-defined printing patterns. In addition, the ink needs to preserve colloidal stability to avoid aggregation of QDs that clogs the printing nozzle eventually.[31,32] Commonly, as synthesized PbS QDs are dispersed in apolar solvents such as hexane, proven to offer colloidal stability.[33,34] Such QDs possess aliphatic ligands on their surfaces to ensure solubility in apolar solvents, which at the same time hinder the electrical charge transport in fabricated solid-state films. Therefore, the native ligands are typically exchanged by a solid-state ligand exchange with small organic molecules, ions, or inorganic complexes to improve the electronic coupling.[35] Dithiols, in particular, are additionally cross-linking the QDs. This makes the film more robust against subsequent solvent treatment and is beneficial for device fabrication such as layer-by-layer deposition reaching thicker QD films.[36]

Certainly, printing PbS QDs from its well-established solvent hexane would be preferable for handling; however, hexane is a highly volatile (low boiling point of 69 °C) and low viscosity (0.3 cP) solvent. Both factors limit its utility for printing, seen as poor drop formation and fast clogging of the printing nozzle.[32] A continuous stream of drops, typically with detrimental satellite droplets, is achieved only briefly by tuning the printing parameters to the limit (applying a high voltage to the nozzle). Hence, printing reproducibly isolated patterns cannot be readily accomplished, but rather continuous QD films with low resolution. Experimentally, we find an improved droplet pinning on HfO_2 rather than SiO_2 oxide substrates, which leads to slightly higher-resolved features (Figure S1, Supporting Information). The optical bright-field microscopy image in **Figure 1**a shows such a printed PbS QDs film on HfO_2. The printing pitch of $p = 30$ μm can be deduced from the spacing between two printed lines. The edge-radius r of the square is about the same as p. The film thickness increases toward the center up to a distance of two times p from the edge. It is worth noting that an isolated pinned single drop dries faster than a larger film pattern's volume. This slower drying of a low viscous solvent steadily increases the spatial QDs concentration and favors a denser packing of the film.[35,37,38] The result is a smoother film morphology having a low root mean square surface roughness R_q of 5 nm (Figure 1b).

To improve the printing resolution and achieve stable drop-on-demand printing, we followed an approach demonstrated for Au nanoparticles by adding α-terpineol[32] that has an increased boiling point (217 °C) as well as viscosity (38 cP), to hexane. For a mole-ratio content from 30 up to 90% of α-terpineol, this co-solvent lies in the introduced jettability window defined by the Ca (capillary number) - We (Weber number) space.[32] The proposed window accounts for inertial and viscous forces, as well as surface tension, governing a stable drop formation. For a colloidally stable ink, though, a high hexane content is to be preferred. Indeed, with a mole-ratio of 60% hexane to 40% α-terpineol and a PbS QDs mass loading of ≈13% (100 mg mL⁻¹) to the ink, single droplets were formed reproducibly. Figure 1c shows the achieved resolution of 50 μm on SiO_2 oxide. The AFM image (Figure 1d) shows a placed droplet with a thickness of ≈220 nm. The co-solvent does introduce an increased root mean square surface roughness of $R_q = 45$ nm, possibly due to increased flow dynamics during evaporation resulting

**ADVANCED
SCIENCE NEWS**

www.advancedsciencenews.com

**ADVANCED
MATERIALS
TECHNOLOGIES**

www.advmattechnol.de

Printed from hexane

Printed from α-terpineol - hexane

Figure 1. Printing resolution comparison between hexane and co-solvent approach. a) The optical microscope image and b) the AFM image show the hexane-printing approach, achieving a smooth film morphology (R_q = 5 nm) with poor printing resolution. The printing pitch of p = 30 μm can be deduced, and fringing indicates a film thickness convergence towards the center of the printed square pattern. Panels (c) and (d) depict the co-solvent approach's superior printing resolution of 50 μm, showing a printed dot pattern. A full PbS QDs coverage is achieved with an improved drop pinning but rougher surface (R_q = 45 nm). The highlighted film profiles (white) are plotted in both AFM images at their exact position.

from high and low boiling point solvents,[31,39] and can lead to agglomerated QDs. However, no coffee ring effect is observed, and a full QDs coverage is reached.
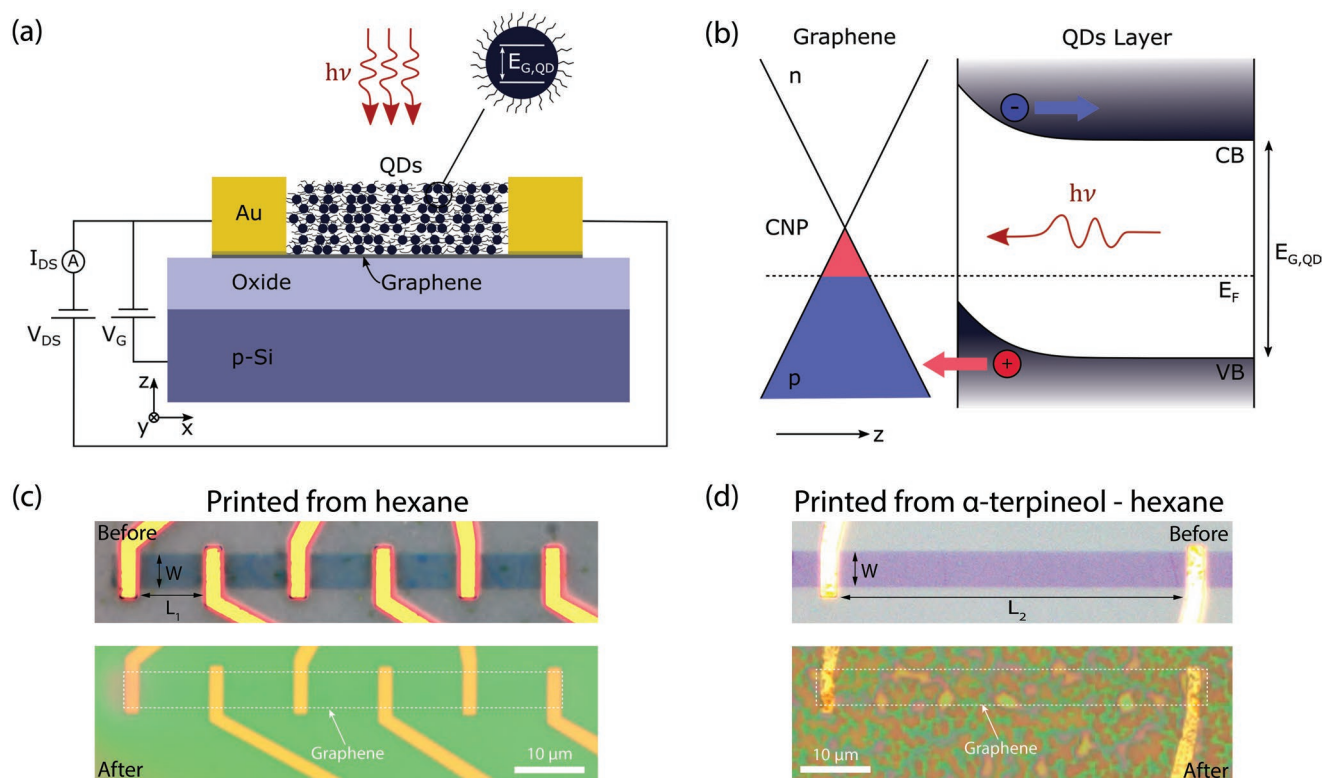
2.2. Printed Hybrid Graphene-PbS QDs Phototransistors on Flat Substrates

Phototransistors are desirable for their gain; the generation of multiple charge carrier per incident photon. Graphene with its outstanding charge carrier mobility and the ease of size-tunable spectral sensitivity of colloidal PbS QDs offers a good match. Combined in a hybrid phototransistor architecture, the detectors demonstrated spectral sensitivity in the NIR to SWIR range at low light levels (below pW).[40,41] **Figure 2**a displays the device schematic of such a hybrid graphene-QDs phototransistor. Most commonly, the graphene field-effect-transistor (FET) is fabricated on a flat and rigid (p-doped Si) substrate with an oxide in between. A source-drain voltage (V_{DS}) is applied to the Au contacts of the patterned graphene channel, while the current (I_{DS}) is measured simultaneously. The PbS QDs film is deposited on top of the graphene channel and defines the spectral sensitivity of the detector. Figure 2b depicts schematically the energy band diagram of the graphene-PbS QDs film junction. The photogating mechanism relies on three main steps: i) the incoming photon is absorbed by the QDs film layer, creating

an exciton (electron-hole pair); ii) the built-in electric field separates the charge carriers; iii) the electrons left in the QDs film result in a photogating of the graphene channel, modulating I_{DS}. This mechanism saturates eventually, as more charge carriers are absorbed in the QDs film layer.

To evaluate the device-level performance of the developed inkjet printing approach, we fabricated hybrid graphene-colloidal PbS QDs phototransistors. Both introduced printing approaches were used to deposit PbS QDs on top of the channels for comparison. Subsequently they are named hexane and co-solvent devices, respectively. The hexane devices are shown in Figure 2c. The graphene FETs have a channel length of L_1 = 10 μm, width of W = 5 μm, and are fabricated on a p-doped Si substrate. The oxide layer consists of 90 nm thermally grown SiO$_2$ oxide with an additional 20 nm of ALD-grown HfO$_2$ on top, which improves the droplet pinning. The uniform color of the PbS QDs film indicates a smooth surface as confirmed by AFM (Figure S2, Supporting Information). In Figure 2d, the co-solvent device is shown with a L_2 = 50 μm and W = 5 μm graphene FET geometry. Due to improved drop formation and pinning on the substrate, a standard p-doped Si with 285 nm of thermally grown SiO$_2$ was used. In agreement with the printing resolution demonstration (Figure 1d), the increased surface roughness gives rise to a color pattern. For the hexane and co-solvent devices, a film thickness of ≈ 100 nm is estimated after a solid-state ligand exchange of the native QD ligands with

Figure 2. Hybrid graphene-PbS QDs phototransistor architecture on commonly used flat substrate. Panel (a) shows the device architecture composed of a graphene FET fabricated on doped silicon (p-Si) with an oxide layer in between. A bias voltage (V_{DS}) and gate voltage (V_G) are applied, while the current between source and drain (I_{DS}) is measured. The energy diagram in panel (b) shows the photogating effect caused by exciton (electron-hole pair) separation. The applied gate voltage controls the charge carrier density in the graphene channel, shifting it above or below the charge neutrality point (CNP) to electron (n-type) or hole (p-type) conduction regimes, respectively. Panels (c) and (d) show optical microscope images of the devices before and after printing PbS QDs on top of the graphene channels for both approaches. The phototransistors have a channel width of $W = 5\,\mu m$ and channel lengths of $L_1 = 10\,\mu m$ and $L_2 = 50\,\mu m$ for the hexane and co-solvent approach, respectively. The differing color of the graphene channel before QDs sensitization is due to the variation in gate oxides of HfO_2 (hexane approach) and SiO_2 (co-solvent approach). The devices were fabricated in two individual non-related batches, which explains their channel geometry variation. The estimated PbS film thickness after a solid-state ligand exchange to 1,2-ethanedithiol is $\approx 100\,nm$ (two printed layers) and $\approx 100\,nm$ (one printed layer) for the hexane and co-solvent printing approach, respectively.
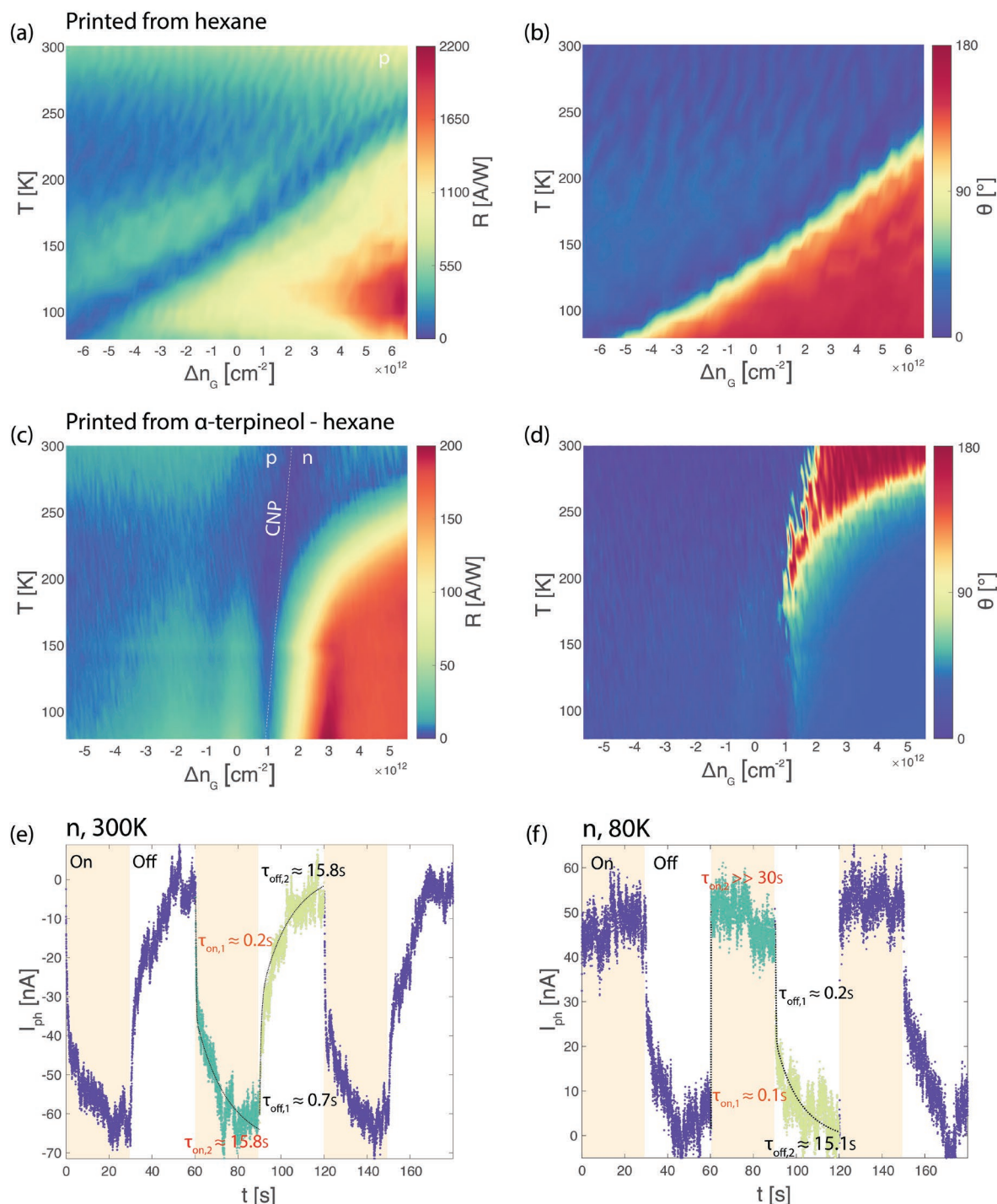
1,2-ethanedithiol (refer to AFM measurements, Figure S2, Supporting Information). Two and one printing layer were required for the hexane and co-solvent devices, respectively. The devices were fabricated in two individual non-related batches, what explains their variation in channel geometry.

After device fabrication, a responsivity map over gate voltage and temperature was acquired to compare the performance of both printing approaches. To account for the different gate oxides, the gate voltage is converted to an induced charge carrier density $\Delta n_G = C_{oxide} / e \cdot V_G$ ($C_{SiO22//HfO2} = 35.3\,nF\,cm^{-2}$, $C_{SiO2} = 11.9\,nF\,cm^{-2}$ (Figures S3, Supporting Information). The incoming monochromatic light was chopped at a frequency $f_{chop} = 5\,Hz$, and the light power P_{in} as well as the photocurrent I_{ph} were measured with a lock-in amplifier (amplitude and phase signal). The responsivity of detectors were calculated using

$$R = \frac{I_{ph}}{P_{in}} \tag{1}$$

Figure 3a,b shows the observed responsivity amplitude and phase signal of the hexane device. A bias of $V_{DS} = 100\,mV$ was

applied, and the wavelength was set to 1180 nm (first excitonic peak of PbS QDs batch for the hexane printing after device integration, Figure S4, Supporting Information) with an irradiance of 125 $\mu W\,cm^{-2}$. The temperature was swept from 300 K down to 80 K and while the applied gate voltage was varied between +/- 30 V ($6.6\times 10^{12}\,cm^{-2}$). The highest performance of 2090 A W^{-1} is observed at $T = 110\,K$ and $\Delta n_G = 6.4\times 10^{12}\,cm^{-2}$ ($V_G = 29\,V$). In comparison, Figure 3c,d shows the map for the co-solvent device. Here, the gate was varied between +/- 75 V ($5.6\times 10^{12}\,cm^{-2}$) with an applied bias of $V_{DS} = 500\,mV$ to account for the longer channel length. The wavelength was set to 1580 nm (first excitonic peak of PbS QDs batch for co-solvent printing after device integration, see **Figure 4**a) at an irradiance of 120 $\mu W\,cm^{-2}$. The dashed white line indicates the graphene channel's charge neutrality point (CNP), and observed for the co-solvent device only. Applying positive or negative gate voltages with respect to the CNP causes electron (n-type) or hole (p-type) conduction due to electric field doping in the graphene channel, respectively. The highest performance of 195 A W^{-1} is observed at $T = 80\,K$ and $\Delta n_G = 2.9\times 10^{12}\,cm^{-2}$ ($V_G = 39\,V$) in the n-type regime of graphene. Interestingly for both devices, a phase shift of 180° is observed when cooling the device down

**ADVANCED
SCIENCE NEWS**

www.advancedsciencenews.com

**ADVANCED
MATERIALS
TECHNOLOGIES**

www.advmattechnol.de

Figure 3. Responsivity maps over gate voltage and temperature for performance comparison of the hexane and co-solvent devices. Panels (a) and (b) show the responsivity amplitude (R) and phase (θ) of the hexane device. The measurement was performed at a bias of $V_{DS} = 100$ mV, a wavelength of $\lambda = 1180$ nm (≈ 4 nm QDs), and irradiance of 125 μW cm^{-2}. $\Delta n_G = C_{oxide}/e \cdot V_G$ indicates the induced charge carrier density by the applied gate voltage and accounts for the different oxides. Panels (c) and (d) show the responsivity of the co-solvent device measured at a bias of $V_{DS} = 500$ mV, a wavelength of $\lambda = 1580$ nm (≈ 6 nm QDs), and irradiance of 120 μW cm^{-2}. The charge neutrality point (CNP) is indicated by the white dashed line, dividing the hole (p-type) and electron (n-type) conduction regimes in the graphene channel, and observed for the co-solvent device only. For both printing approaches, the highest values are reached at low temperatures and accompanied by photoresponse sign change (phase jump of 180°). The time traces highlight this sign change from a e) negative to a f) positive photocurrent for the co-solvent device and are measured at a bias $V_{DS} = 500$ mV, wavelength of $\lambda = 1580$ nm, and irradiance of 7 μW cm^{-2}. The fitted time constants indicate a faster response ($\tau_{on,1} \downarrow$) and a slower detrapping from charge traps ($\tau_{on,2} \uparrow$) upon turning on the light, if the device is cooled from 300 to 80 K.
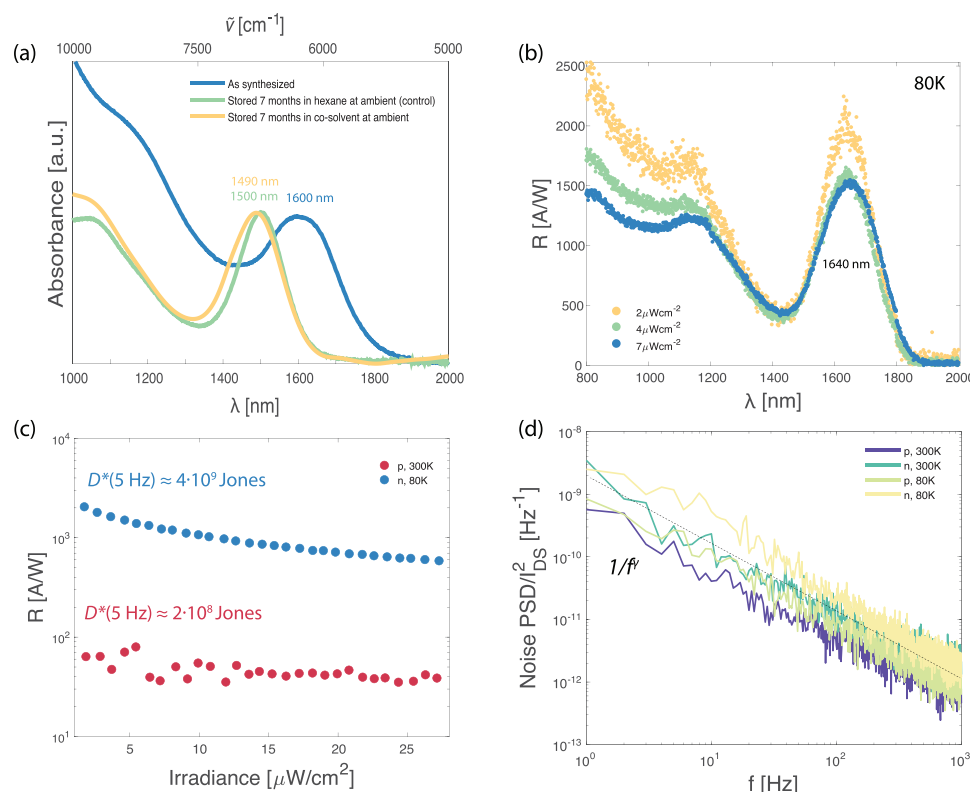
Figure 4. Performance of the co-solvent device. a) shows the colloidal stability of the QDs dispersed in the co-solvent ink over a time period of 7 months. The spectra were acquired with the QDs dispersed in tetrachloroethylene (TCE). A ≈ 100 nm blue shift of the first excitonic peak compared to the as synthesized QDs can be explained by oxidation, as the ink was stored at ambient conditions and is observed for the control ink stored in hexane too. After device integration in panel (b), the PbS QDs preserve their first excitonic peak (n-type regime at 80 K, f_{chop} = 5 Hz, V_{DS} = 500 mV). Hybrid graphene-PbS QDs phototransistors are sensitive to irradiance levels. In panel (c), the $R \sim$ Irradiance^{-1} relation is highlighted (f_{chop} = 5 Hz, V_{DS} = 500 mV). d) shows the current normalized noise spectra of the device in the main operation points. The spectra were acquired with a bias of V_{DS} = 100 mV and averaged over 10 s.

from 300 to 80 K. This is in good agreement with previously reported photoresponse sign flipping upon cooling down the device.[24]

The observed higher responsivity values of the hexane device can be explained manifold. The devices are fabricated in two individual batches why device-to-device variation can not be excluded in general. This comprises the graphene channel (field effect mobilities ≈ 350 for the hexane device and 1500 cm^2 Vs^{-1} for the co-solvent device booth at 300 K, Figure S5, Supporting Information), PbS QDs synthesis and their size (≈4 nm for hexane device and ≈ 6 nm QDs for the co-solvent device estimated from absorption spectra[42]), as well as the ligand exchange. However, we would like to indicate that a smoother film morphology can point to denser QDs packing in the film. This is preferential as it reduces dot-to-dot distance and facilitates an enhanced electrical coupling between them.[35,43] Moreover, it also indicates fewer voids and agglomerations of QDs that could host residual species introducing traps and increasing the energy disorder deteriorating the charge transport across the film,[44,45] as shown in the literature.[46–48]

Balancing the viscosity and pinning of the droplet on the substrate can be important to achieve densely packed QDs film while ensuring the printing of fine features. At this point, the better droplet pinning and printing stability of the co-solvent

approach is important to extend this technological approach to a variety of substrate materials and shapes. We thus investigate the co-solvent device in further detail and focus on photocurrent time traces in the n-type regime of graphene (irradiance of 7 μW cm^{-2}). At 300 K a negative photocurrent is observed (Figure 3e), following the room temperature responses reported in the literature (see Figure 2b);[23,24,40,41,49] the negatively charged QDs film upon light exposure, induces a positive charge reducing the graphene channel's electron charge density. However at 80 K, in Figure 3f, the photocurrent is positive, suggesting a net positively charged QDs film. This implies an energy rearrangement of the graphene-QDs film interface, and is supported by time constant changes of fitted double exponential function $f(t) = A_{on,1} \cdot e^{-t/\tau_{on,1}} + A_{on,2} \cdot e^{-t/\tau_{on,2}}$ to the photocurrent (Figure 3e,f). Upon cooling the device down to 80 K, the light on time constant $\tau_{on,2}$ increases from 15.8 to much larger than 30 s (measuring time), while $\tau_{on,1}$ goes down at the detection limit from 0.2 to 0.1 s. We assign the faster time constant $\tau_{on,1}$ to the separation of the electron-hole pairs, hence, indicating a faster device response at reduced temperatures. In contrast, the population of trapped states on the QDs surface can be assigned to the slower time constant $\tau_{on,2}$. The increased population rate of those traps at lower temperatures changes the Fermi level in the QDs film. This readjustment at

**ADVANCED
SCIENCE NEWS**

www.advancedsciencenews.com

**ADVANCED
MATERIALS
TECHNOLOGIES**

www.advmattechnol.de

the interface causes an electron flow to graphene, thus, leading to the photocurrent sign change. We note that the Fermi level of the QDs film readjusts around the middle of the band gap and leads to accessible charge transfer in the p-type and n-type regimes of graphene. As a result positive photocurrents ($\theta = 0°$) are observed on both sides.

In the responsivity maps over gate voltage and temperature, the light irradiance was kept at a high level to emphasize the observed sign-flipping features. In Figure 4, we now focus on the performance of the co-solvent device at lower light levels. The device integration preserves the first excitonic peak (Figure 4(a) to (b)). In addition, the QDs ink shows colloidal stability over 7 months (Figure 4a). The ~ 100 nm blue shift of the first excitonic peak can be explained by oxidation as the QDs were kept in ambient conditions,[50–54] and it is also observed in the control ink stored in hexane under ambient condition. The spectral photoresponse was measured in the n-type regime of graphene at 80 K (highest photoresponse point), at a bias of $V_{DS} = 500$ mV, and $f_{chop} = 5$ Hz light modulation. Reducing the light irradiance to ≈ 1 μ W cm^{-2} increases the responsivity by one order of magnitude to $\approx 1 \times 10^3$ A W^{-1}. This $R \sim$ Irradiance^{-1} dependency is highlighted in Figure 4c for p-type regime at 300 K (red) and n-type regime at 80 K (blue). Moreover, in Figure 4d, the characteristic low-frequency $1/f^\gamma$ dependence of graphene is depicted. The spectra are normalized by the source-drain current I_{DS} to account for different charge carrier densities in the graphene channel. Further normalization by the channel geometry (5×50 μm^2) results in noise values in the range of $\approx 10^{-8}$–10^{-7} μm^{2}Hz^{-1} at 10 Hz. Together with fitted γ values in the range of 1–1.3, this agrees well with commonly reported values in the literature.[55] At 5 Hz (f_{chop}) a noise current of 525 pA for p-type at 300 K (measured $I_{DS} = 52.9$ μA) and 745 pA for n-type regime at 80 K (measured $I_{DS} = 23.9$ μA) is estimated. With

$$D^* = \frac{R\sqrt{A\Delta f}}{I_{noise}} \tag{2}$$

where A is the detector area, and Δf is the frequency bandwidth, specific detectivities D^* of 2×10^8 (p-type, 300 K) and 4×10^9 Jones (n-type regime, 80 K) can be estimated at 5 Hz modulation and a wavelength of 1.6 μm. However, taking into account that the detector becomes faster at low temperatures (reduced $\tau_{on,1}$), the photocurrent reaches 6 nA after 1 ms, and hence, with the lower noise at 1 kHz, a D* of at least 1×10^{10} Jones is reached. The highest reported detectivities for this type of devices are in the range of $D^* \approx 10^{12}$–10^{13} Jones[40,56] and based on layer by layer spin coated PbS QDs films. This approach is expected to result in a lower density of traps and thus gives superior charge transport performance in the PbS film. In contrast to printing, though, it is not applicable to curved substrates.

The highest photoresponse of the co-solvent devices shifts from p-type to the n-type region of the graphene channel if the device is cooled from 300 down to 80 K (Figure 3c). This one order of magnitude improvement is not supported by reduced noise upon cooling (Figure 4c). Keeping in mind that the highest photoresponse shift is accompanied by a transferred charge carrier type change across the QDs-graphene interface from holes (300 K) to electrons (80 K), it indicates an improved charge transfer of electrons rather than holes. Recently, an enhanced photoresponse in graphene-PbS QDs hybrid device, with tetrabutylammonium iodide (TBAI) capped ligands, was observed introducing a ZnO layer to facilitate the electron transport to graphene.[57] The enhanced charge collection is in good agreement with observed higher electron mobility values leading to longer diffusion depths ($L_D \sim \sqrt{\mu}$) in those QDs films.[58]

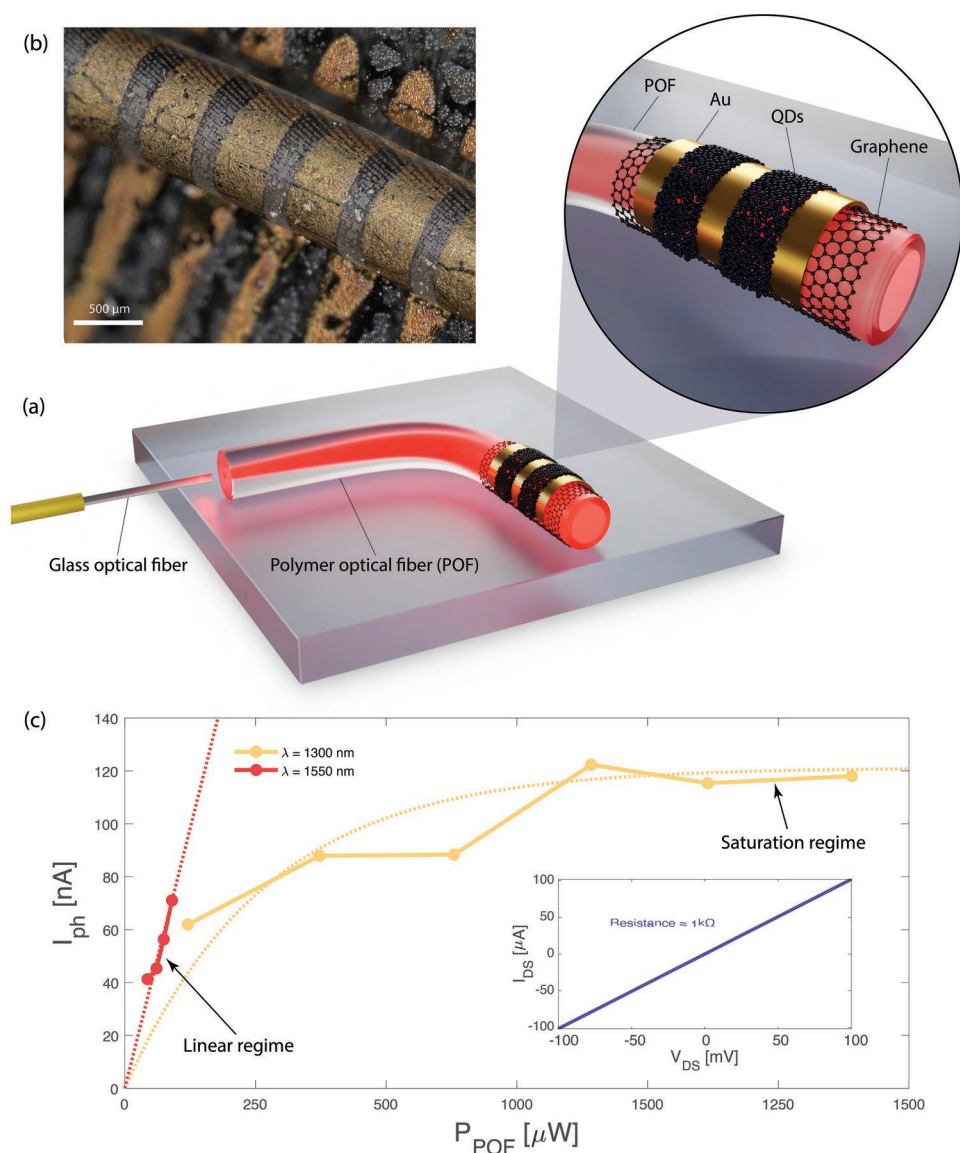## 2.3. Detector on Curved Substrate

Conformal manufacturing of the printed hybrid graphene-PbS QDs photodetectors was demonstrated by the fabrication of a device on a curved surface (POF). POFs are commonly used in photonic textile sensors for healthcare applications. Such sensors have advantages related to their immunity to electromagnetic fields, mechanical robustness, as well as the capability of multiplexing and multifunctionality.[14] However, they require converting the optical signal to an electrical one, which brings disadvantages such as the need for additional bulky elements (light source, photodetector). Here, we show the seamless integration of a photodetector to an elastomeric POF that was recently proposed as wearable sensors for pressure and movement sensing.[59,60]

The zoom-in image of **Figure 5**a shows the device in more detail. By carefully fishing graphene, it was wrapped around the POF of 1 mm in diameter. Special care was taken by adding slow rotation to the POF while the DI water level was lowered manually. Au contacts were then evaporated using a shadow mask with a spacing of 250 μm. Finally, the co-solvent printing approach was used to deposit PbS QDs only on the graphene-covered areas (two printing layers), leaving the rest of the fiber untouched. The optical microscope image in Figure 5b shows the final structure. We note that the superior pinning of the co-solvent printing approach is crucial at this point and could potentially ensure printing on a variety of different substrate materials and geometries.

The hybrid device acts as a functional coating and detects light propagating through the fiber without interfering with the light path (Figure 5a). A single-mode fiber couples laser light to the multimode POF, where out scattered light is detected. Figure 5c shows the photocurrent for the two telecom wavelengths 1300 nm (O band) and 1550 nm (C band) by varying the coupled light power $P_{coupled}$ between 0.2 and 2.7 mW. In particular, we find higher photocurrents for the 1300 nm laser excitation reaching 120 nA at 1.7 mW of coupled light. A photocurrent of 70 nA is reached for 1550 nm laser excitation at a $P_{coupled}$ of 1.5 mW. It has to be noted that the polysiloxane-based POF has a spectral dependence.[59,61,62] We find a 0.4 and 2.3 dB cm^{-1} attenuation for light coupled at 1300 and 1550 nm to the POF, respectively. In addition, a coupling loss and a bending loss of 0.4 dB each are observed. With a POF length of 5 cm, the power at the detector position inside the POF is estimated using

$$P_{POF} = P_{coupled} \times 10^{-\alpha_{dB}/10} \tag{3}$$

where $P_{coupled}$ is the light power coupled to the fiber, and α_{dB} is the attenuation expressed in dB. The reduced laser power

**ADVANCED
SCIENCE NEWS**

www.advancedsciencenews.com

**ADVANCED
MATERIALS
TECHNOLOGIES**

www.advmattechnol.de

Figure 5. Demonstration of the hybrid-PbS QDs phototransistor on a curved surface. Panels (a) and (b) show the device's schematic and optical microscope image, respectively. Graphene was wrapped around a polymer optical fiber (POF) of 1 mm in diameter. Au contacts were deposited on top of the graphene channel, and the PbS QDs were printed on this curved surface by the co-solvent approach. The fabricated device detects outscattered light upon laser excitation without interrupting the light path. Panel (c) shows the photocurrent of this functional coating to the POF ($V_{DS} = 100$ mV). The POF has a spectral absorbance, which is why similar in-coupled light powers for the 1300 and 1550 nm wavelength vary in the power next to the detector P_{POF}. In combination with the graphene channel resistance of 1 kΩ (inset), the photogating is confirmed as the photocurrent trend in the linear regime shows a higher sensitivity $R' = I_{ph}/P_{POF}$ for 1550 nm wavelength excitation (first excitonic peak of the QDs). Note that $R' \sim R$ but includes the wavelength-dependent out-scattering behavior of the POF to the responsivity R.

reaching the detector at 1550 nm wavelength reveals the expected wavelength dependence. As $I_{ph} = R \cdot P_{in}$, a linear trend is expected for the photocurrent with $I_{ph} = R' \cdot P_{POF}$. Note that $R' \sim R$ but describes the responsivity capturing also the light-outscattering behavior of the POF itself. However, comparing the two slopes in the linear regime, a higher photoresponse is expected at compatible light powers for the 1550 nm rather than the 1300 nm wavelength excitation. This agrees well with the higher spectral response around the first excitonic peak observed in the device fabricated on the flat substrate (see Figure 4b). In

contrast, the more light power reaching the detector at 1300 nm causes a device operation in the photocurrent saturation regime. The saturation effect is caused by the increasing number of photogenerated charge carriers at the QDs-graphene interface, lowering the built-in potential and, hence, counteracting the exciton charge separation.[40] The $I–V$ curve shown in the inset reveals a graphene channel resistance of $\approx$1 kΩ. In combination with the spectral dependence, this confirms the expected photogating effect; where the channel current is measured and the spectral sensitive QDs modulate the channel resistance.

3. Conclusion

This study demonstrates the potential of graphene-PbS QDs hybrid IR phototransistors to overcome the geometrical restriction of a flat substrate using conformal manufacturing. To locally functionalize a POF fiber of 1 mm in diameter, graphene was wrapped around it, and PbS QDs were, subsequently, inkjet printed on top of the contacted graphene devices. Confirmed by a low electrical resistance (1 kΩ) and the spectral sensitivity of the photoresponse (higher photoresponse at first excitonic peak), this functional coating detects light by the photogating effect without interrupting the light path along the waveguide. A α-terpineol and hexane co-solvent ink was developed to print on top of such a curved surface. The ink showed colloidal stability over at least 7 months, and a printing resolution of 50 µm was achieved on a common flat substrate. The detector fabricated on the flat substrate demonstrates responsivity values $R \approx 1 \times 10^3$ A W^{-1} (irradiance ≈ 1 µW cm^{-2}) and a detectivity of at least $D^* \approx 1 \times 10^{10}$ Jones at 1.6 µm. By performing responsivity maps over gate voltage and temperature, we confirm our previously reported photocurrent sign-flipping that we assign to an increased population rate of trap states at the QDs surface if the device is cooled down to 80 K. The observed photoresponse improvement upon cooling the detector is not supported by lower noise characteristics of the graphene channel but a faster photoresponse at 80 K compared to 300 K. This faster response, in combination with the photocurrent sign-flipping indicates an enhanced charge carrier collection for electrons rather than holes across the QDs film-graphene interface. The co-solvent printing approach was compared to printing PbS QDs dispersed in hexane only, confirming poor printing properties but an overall smoother film morphology. A device level comparison indicates that smoother PbS QDs absorber films might improve the device performance, possibly by increasing the charge carrier diffusion length due to the denser QDs packing. The extension of the graphene-PbS QDs hybrid architecture to curved surfaces by conformal manufacturing is a first step towards integrating this cost-effective and variable technology into e-textiles, where a single fiber can support multiple functionalities.

4. Experimental Section

Graphene Growth and Transfer: CVD graphene was grown as reported previously,[63,64] with slight adaptations. The commercial copper foil (Foil 2017, No. 46365, Alfa Aesar) was cleaned in acetone (15 min), isopropanol rinsed (IPA), N$_2$ dried, nitric acid (90 s), two times DI-water (1 min), ethanol (1 min), and blown dried with N$_2$ before a reduction annealing in H$_2$-rich atmosphere (20 sccm H$_2$ in 200 sccm Ar) at 1000 °C and < 1 mbar for 90 min. An addition of 0.05 sccm CH$_4$ to the chamber for 25 min initiated the graphene growth.

Cu-Etching for Graphene Transfer: For graphene transfer, PMMA 50K-protected graphene on copper was placed in the Cu-Transene etchant for 1 h. Then, after rinsing in DI water, it was put into hydrochloric acid (10%) for 5 min and rinsed again with DI water. Finally, graphene was fished on the desired substrate from DI water.

Common Device Fabrication on Flat Substrate: The detailed fabrication is described in the Supporting Information. But briefly, highly p-doped Si with 285 nm chlorinated dry thermal SiO$_2$ or p-doped Si with 90 nm chlorinated dry thermal SiO$_2$ and 20 nm of ALD grown HfO$_2$ was used

as a substrate. CVD graphene was fished from H$_2$O and patterned lithographically by O$_2$ plasma etch. Au contacts were deposited using lithography and a lift-off procedure.

POF Device Fabrication: The detailed process of the PDMS-based POFs is described elsewhere,[59,60] but briefly; a PDMS formulation was injected into a tubular mould, cured in the oven, and demoulded. For the detector fabrication, graphene was carefully fished from H$_2$O. The POF was put on a glass support inside the H$_2$O containing beaker. The freestanding end was slowly rotated using a tweezer, while the H$_2$O level was lowered gently with a pipet. A slow rotation was added once the graphene touched the fiber, wrapping it around the POF. After drying at ambient overnight, the POF was put into a vacuum for 48 h (3 mbar). For contact evaporation, the POF was fixed to a glass slide and covered with an aluminum shadow mask (15 µm thick). Cr (2 nm) and Au (200 nm) were deposited by electron-beam evaporation as top contacts to graphene.

PbS QDs Synthesis and Ink Prepration: PbS QDs were synthesized according to the method of Hines et al.[33] with slight modifications and described in detail in the Supporting Information. For the co-solvent printing approach, a 60% to 40% mole-ratio of hexane to α-terpineol solvent mixture was prepared. The QDs were dispersed in the co-solvent with a 100 mg mL^{-1} concentration (mass concentration of the final ink). A lower concentration of 50 mg mL^{-1} dispersion of PbS QDs in hexane was used for the hexane-printing approach to slow down the clogging of the nozzle. Before printing, the QDs inks were filtered with a 0.45 µ PTFE filter.

PbS QDs Inkjet Printing and Ligand Exchange: Printing was performed with a LP50 inkjet printer using Dimatix disposable cartridges with 1 pl nozzle volume. A drop spacing of 30 µm (800 dpi) was chosen to ensure pinhole-free printed films. Subsequently, the films were dried for 10 min on a hot plate at 60 °C to ensure solvent evaporation. For the co-solvent printing approach only, a H$_2$O rinse was performed to ensure the cleaning of α-terpineol from the film. Next, ligands were exchanged by putting a 100 µl droplet of 2 vol% 1,2-ethanedithiol in acetonitrile for 60 s onto the sample, whereafter, the sample was spun at 2500 rpm for 45 s. Finally, a 100 µl droplet of acetonitrile is placed on the sample and spun at 2500 rpm for 45 s immediately.

Electrical Characterization: Electrical characterization was performed with a Keithley 4200-SCS semiconductor characterization system. The oxide capacitance was characterized by applying an RMS amplitude of $V_{rms} = 100$ mV at a frequency $f = 100$ kHz, while the DC bias is swept between +/- 5 V. The conductance of the graphene transistors was measured in two-probe configurations. The field-effect mobility µ was estimated by linear least squares fitting to the transfer curve (I_{DS} vs V_G) according to $\mu = \frac{L}{W V_{DS} C_G} \frac{dI_{DS}}{dV_G}$, where L and W are the channel length and width, V_{DS} and I_{DS} the source-drain bias voltage and measured current, C_G the oxide capacitance per area, and V_G the applied gate voltage.

Photoresponse: A broadband light source (Thorlabs, SLS201) was optically modulated with a chopper (Thorlabs, MC2000B-EC) and focused onto and monochromator (Princeton Instruments, SpectraPro HRS-300 spectrometer with grating 150 G mm^{-1}, blaze 0.8 µm). Long pass filters attenuated the higher spectral orders (400, 600, 800, 1200, and 1900 nm). The monochromated light was collimated with a lens and split with a 50/50 Polkadot beamsplitter onto a reference detector (Gentec, UM-9B-L). The samples were placed into an optically accessible cryostat (JANIS ST-100) with a quartz glass window and cooled with liquid nitrogen at a base pressure of 3× 10^{-7} mbar. Gate voltage and source-drain bias was applied with two SMUs (Keithley, 2614B and 2450). The photovoltage of the reference detector was measured with a lock-in amplifier (Stanford Research System, SR865A). In contrast, the photocurrent of the sample was measured using a shunt resistance of 100 Ω, also with a lock-in amplifier (Stanford Research System, SR865A). The photoresponse of the detector fabricated on the POF was evaluated using a transimpedance amplifier (Stanford Research System, SR570). Lasers with 1300 nm (Newport, TLB-6724) and 1550 nm (New Focus, TLB-6328) excitation wavelengths were used.

Noise Characterization: A battery-powered transimpedance amplifier (Stanford Research Systems, SR570) was used for the noise measurements. The samples were measured in dark and at a base pressure of 3×10^{-7} mbar. The signal was low pass filtered (10 kHz) and measured with a data acquisition board (National Instruments, USB6341) at a sampling rate of 500 kHz. The DC offset was removed, and power spectral densities of 10 one-second-long time traces were estimated and subsequently averaged.

Atomic Force Microscopy: The measurements were performed with a Bruker Dimension ICON 3 in Scanasyst peak force tapping mode.

Supporting Information

Supporting Information is available from the Wiley Online Library or from the author.

Conflict of Interest

The authors declare no conflict of interest.

Author Contributions

G.K. and I.S. designed the study and planned the experiments with inputs and discussion by M.C. and M.K. G.K. fabricated the graphene devices, formulated the ink for printing, performed ligand exchange treatments, worked on the measurement setups, and performed all the measurements with inputs from I.S. and D.B. Graphene was grown by R.F. The QDs were synthesized by M.G. and D.D. with inputs and discussion by M.K. Inkjet printing was performed by S.B. with inputs and discussion from Y.R. The POF was fabricated by K.S. with inputs and discussions by L.B. and R.R. The paper was written by G.K with contributions from all authors.

Data Availability Statement

The data that support the findings of this study are available from the corresponding author upon reasonable request.

Keywords

colloidal quantum dots, conformal manufacturing, e-textiles, graphene, infrared photodetectors, inkjet printing, polymer optical fibers

[1] Y. Khan, A. E. Ostfeld, C. M. Lochner, A. Pierre, A. C. Arias, *Adv. Mater.* **2016**, *28*, 4373.

[2] Y. Liu, M. Pharr, G. A. Salvatore, *ACS Nano* **2017**, *11*, 9614.

[3] T. R. Ray, J. Choi, A. J. Bandodkar, S. Krishnan, P. Gutruf, L. Tian, R. Ghaffari, J. A. Rogers, *Chem. Rev.* **2019**, *119*, 5461.

[4] D. Jaque, C. Richard, B. Viana, K. Soga, X. Liu, J. García Solé, *Adv. Opt. Photonics* **2016**, *8*, 1.

[5] E. Vavrinsky, N. E. Esfahani, M. Hausner, A. Kuzma, V. Rezo, M. Donoval, H. Kosnacova, *Biosensors* **2022**, *12*, 217.

[6] C. M. Lochner, Y. Khan, A. Pierre, A. C. Arias, *Nat. Commun.* **2014**, *5*, 5745.

[7] E. O. Polat, G. Mercier, I. Nikitskiy, E. Puma, T. Galan, S. Gupta, M. Montagut, J. J. Piqueras, M. Bouwens, T. Durduran, G. Konstantatos, S. Goossens, F. Koppens, *Sci. Adv.* **2019**, *5*, eaaw7846.

[8] X. Xu, S. Xie, Y. Zhang, H. Peng, *Angew. Chem., Int. Ed.* **2019**, *58*, 13643.

[9] J. Choi, Y. Jung, S. J. Yang, J. Y. Oh, J. Oh, K. Jo, J. G. Son, S. E. Moon, C. R. Park, H. Kim, *ACS Nano* **2017**, *11*, 7608.

[10] J. He, C. Lu, H. Jiang, F. Han, X. Shi, J. Wu, L. Wang, T. Chen, J. Wang, Y. Zhang, H. Yang, G. Zhang, X. Sun, B. Wang, P. Chen, Y. Wang, Y. Xia, H. Peng, *Nature* **2021**, *597*, 57.

[11] K. Cherenack, C. Zysset, T. Kinkeldei, N. Münzenrieder, G. Tröster, *Adv. Mater.* **2010**, *22*, 5178.

[12] A. Leber, C. Dong, R. Chandran, T. Das Gupta, N. Bartolomei, F. Sorin, *Nat. Electron.* **2020**, *3*, 316.

[13] X. Shi, Y. Zuo, P. Zhai, J. Shen, Y. Yang, Z. Gao, M. Liao, J. Wu, J. Wang, X. Xu, Q. Tong, B. Zhang, B. Wang, X. Sun, L. Zhang, Q. Pei, D. Jin, P. Chen, H. Peng, *Nature* **2021**, *591*, 240.

[14] B. M. Quandt, L. J. Scherer, L. F. Boesel, M. Wolf, G. L. Bona, R. M. Rossi, *Adv. Healthcare Mater.* **2015**, *4*, 330.

[15] D. Akinwande, D. Kireev, *Nature* **2019**, *576*, 220.

[16] C. Wang, K. Xia, H. Wang, X. Liang, Z. Yin, Y. Zhang, *Adv. Mater.* **2019**, *31*, 9.

[17] Y. Khan, A. Thielens, S. Muin, J. Ting, C. Baumbauer, A. C. Arias, *Adv. Mater.* **2020**, *32*, 15.

[18] W. Zhang, L. Zhang, Y. Liao, H. Cheng, *Int. J. Extreme Manuf.* **2021**, *3*, 4.

[19] M. Böberl, M. V. Kovalenko, S. Gamerith, E. J. List, W. Heiss, *Adv. Mater.* **2007**, *19*, 3574.

[20] A. Yousefiamin, N. A. Killilea, M. Sytnyk, P. Maisch, K. C. Tam, H. J. Egelhaaf, S. Langner, T. Stubhan, C. J. Brabec, T. Rejek, M. Halik, K. Poulsen, J. Niehaus, A. Köck, W. Heiss, *ACS Nano* **2019**, *13*, 2389.

[21] R. Sliz, M. Lejay, J. Z. Fan, M. J. Choi, S. Kinge, S. Hoogland, T. Fabritius, F. P. Garciá De Arquer, E. H. Sargent, *ACS Nano* **2019**, *13*, 11988.

[22] J. Ahn, S. Jeon, H. K. Woo, J. Bang, Y. M. Lee, S. J. Neuhaus, W. S. Lee, T. Park, S. Y. Lee, B. K. Jung, H. Joh, M. Seong, J. H. Choi, H. G. Yoon, C. R. Kagan, S. J. Oh, *ACS Nano* **2021**, *15*, 15667.

[23] M. J. Grotevent, C. U. Hail, S. Yakunin, D. N. Dirin, K. Thodkar, G. Borin Barin, P. Guyot-Sionnest, M. Calame, D. Poulikakos, M. V. Kovalenko, I. Shorubalko, *Adv. Opt. Mater.* **2019**, *7*, 1900019.

[24] M. J. Grotevent, C. U. Hail, S. Yakunin, D. Bachmann, G. Kara, D. N. Dirin, M. Calame, D. Poulikakos, M. V. Kovalenko, I. Shorubalko, *ACS Appl. Mater. Interfaces* **2021**, *13*, 848.

[25] M. J. Grotevent, C. U. Hail, S. Yakunin, D. Bachmann, M. Calame, D. Poulikakos, M. V. Kovalenko, I. Shorubalko, *Adv. Sci.* **2021**, *8*, 2003360.

[26] X. Tang, M. M. Ackerman, G. Shen, P. Guyot-Sionnest, *Small* **2019**, *15*, 1804920.

[27] H. Y. Kim, H. J. Lee, B. H. Kang, *J. Colloid Interface Sci.* **2002**, *247*, 372.

[28] N. Le Grand, A. Daerr, L. Limat, *J. Fluid Mech.* **2005**, *541*, 293.

[29] J. Park, J. Kim, S. Y. Kim, W. H. Cheong, J. Jang, Y. G. Park, K. Na, Y. T. Kim, J. H. Heo, C. Y. Lee, J. H. Lee, F. Bien, J. U. Park, *Sci. Adv.* **2018**, *4*, eaap984.

[30] R. Yin, Z. Xu, M. Mei, Z. Chen, K. Wang, Y. Liu, T. Tang, M. K. Priydarshi, X. Meng, S. Zhao, B. Deng, H. Peng, Z. Liu, X. Duan, *Nat. Commun.* **2018**, *9*, 2334.

[31] B. Derby, *Annu. Rev. Mater. Res.* **2010**, *40*, 395.

[32] H. C. Nallan, J. A. Sadie, R. Kitsomboonloha, S. K. Volkman, V. Subramanian, *Langmuir* **2014**, *30*, 13470.

[33] M. A. Hines, G. D. Scholes, *Adv. Mater.* **2003**, *15*, 1844.

[34] L. Cademartiri, J. Bertolotti, R. Sapienza, D. S. Wiersma, G. Von Freymann, G. A. Ozin, *J. Phys. Chem. B* **2006**, *110*, 671.

[35] D. V. Talapin, J.-s. Lee, M. V. Kovalenko, E. V. Shevchenko, *Chem. Rev.* **2010**, *110*, 389.

[36] W. M. Lin, M. Yarema, M. Liu, E. Sargent, V. Wood, *Chimia* **2021**, *75*, 398.

[37] H.-Y. Ko, J. Park, H. Shin, J. Moon, *Chem. Mater.* **2004**, *16*, 4212.

[38] W. Chen, H. Tang, N. Li, M. A. Scheel, Y. Xie, D. Li, V. Körstgens, M. Schwartzkopf, S. V. Roth, K. Wang, X. W. Sun, P. Müller-Buschbaum, *Nanoscale Horiz.* **2020**, *5*, 880.

[39] J. A. Lim, W. H. Lee, H. S. Lee, J. H. Lee, Y. D. Park, K. Cho, *Adv. Funct. Mater.* **2008**, *18*, 229.

[40] G. Konstantatos, M. Badioli, L. Gaudreau, J. Osmond, M. Bernechea, F. P. G. De Arquer, F. Gatti, F. H. Koppens, *Nat. Nanotechnol.* **2012**, *7*, 363.

[41] Z. Sun, Z. Liu, J. Li, G. A. Tai, S. P. Lau, F. Yan, *Adv. Mater.* **2012**, *24*, 5878.

[42] I. Moreels, K. Lambert, D. Smeets, D. De Muynck, T. Nollet, J. C. Martins, F. Vanhaecke, A. Vantomme, C. Delerue, G. Allan, Z. Hens, *ACS Nano* **2009**, *3*, 3023.

[43] Y. Liu, M. Gibbs, J. Puthussery, S. Gaik, R. Ihly, H. W. Hillhouse, M. Law, *Nano Lett.* **2010**, *10*, 1960.

[44] S. Kahmann, M. A. Loi, *Appl. Phys. Rev.* **2020**, *7*, 4.

[45] G. Shi, H. Wang, Y. Zhang, C. Cheng, T. Zhai, B. Chen, X. Liu, R. Jono, X. Mao, Y. Liu, X. Zhang, X. Ling, Y. Zhang, X. Meng, Y. Chen, S. Duhm, L. Zhang, T. Li, L. Wang, S. Xiong, T. Sagawa, T. Kubo, H. Segawa, Q. Shen, Z. Liu, W. Ma, *Nat. Commun.* **2021**, *12*, 4381.

[46] I. J. Kramer, J. C. Minor, G. Moreno-Bautista, L. Rollny, P. Kanjanaboos, D. Kopilovic, S. M. Thon, G. H. Carey, K. W. Chou, D. Zhitomirsky, A. Amassian, E. H. Sargent, *Adv. Mater.* **2015**, *27*, 116.

[47] F. Ahmed, M. L. Kelley, M. V. Chandrashekhar, A. B. Greytak, *J. Phys. Chem. C* **2021**, *125*, 17796.

[48] C. Wei, W. Su, J. Li, B. Xu, Q. Shan, Y. Wu, F. Zhang, M. Luo, H. Xiang, Z. Cui, H. Zeng, *Adv. Mater.* **2022**, *34*, 2107798.

[49] R. Wang, Y. T. Zhang, H. Y. Wang, X. X. Song, L. F. Jin, J. Q. Yao, *IEEE Photonics J.* **2015**, *7*, 4500706.

[50] J. J. Peterson, T. D. Krauss, *Phys. Chem. Chem. Phys.* **2006**, *8*, 3851.

[51] H. Choi, J. H. Ko, Y. H. Kim, S. Jeong, *J. Am. Chem. Soc.* **2013**, *135*, 5278.

[52] J. M. Luther, M. Law, Q. Song, C. L. Perkins, M. C. Beard, A. J. Nozik, *ACS Nano* **2008**, *2*, 271.

[53] Q. Dai, Y. Wang, Y. Zhang, X. Li, R. Li, B. Zou, J. T. Seo, Y. Wang, M. Liu, W. W. Yu, *Langmuir* **2009**, *25*, 12320.

[54] M. Sykora, A. Y. Koposov, J. A. McGuire, R. K. Schulze, O. Tretiak, J. M. Pietryga, V. I. Klimov, *ACS Nano* **2010**, *4*, 2021.

[55] A. A. Balandin, *Nat. Nanotechnol.* **2013**, *8*, 549.

[56] S. Goossens, G. Navickaite, C. Monasterio, S. Gupta, J. J. Piqueras, R. Pérez, G. Burwell, I. Nikitskiy, T. Lasanta, T. Galán, E. Puma, A. Centeno, A. Pesquera, A. Zurutuza, G. Konstantatos, F. Koppens, *Nat. Photonics* **2017**, *11*, 366.

[57] S. Ahn, W. Chen, M. A. Moreno-Gonzalez, M. Lockett, J. Wang, O. Vazquez-Mena, *Adv. Electron. Mater.* **2020**, *6*, 2000014.

[58] M. J. Speirs, D. N. Dirin, M. Abdu-Aguye, D. M. Balazs, M. V. Kovalenko, M. A. Loi, *Energy Environ. Sci.* **2016**, *9*, 2916.

[59] K. Sharma, E. Morlec, M. Camenzind, R. Rossi, F. Sorin, L. F. Boesel, **2022**.

[60] L. Bahin, M. Tourlonias, M.-A. Bueno, K. Sharma, R. M. Rossi, Smart Textiles with Polymer Optical Fibre Implementation for In-Situ Measurements of Compression and Bending, Sensors and Actuators A: Physical, Volume *350*, **2023**, 114117.

[61] E. Zgraggen, Fabrication and System Integration of Single-Mode Polymer Optical Waveguides, **2014**.

[62] D. Cai, H. M. Heise, *Molecular Spectroscopy—Experiment and Theory*, Springer International Publishing, Cham, Switzerland **2019**, pp. 401–425.

[63] O. Braun, J. Overbeck, M. El Abbassi, S. Käser, R. Furrer, A. Olziersky, A. Flasby, G. Borin Barin, Q. Sun, R. Darawish, K. Müllen, P. Ruffieux, R. Fasel, I. Shorubalko, M. L. Perrin, M. Calame, *Carbon* **2021**, *184*, 331.

[64] O. Schmuck, D. Beretta, R. Furrer, J. Oswald, M. Calame, *AIP Adv.* **2022**, *12*, 055312.